Title
Multiscale analysis of nanoindentation-induced defect structures in gum metal

Authors
Sankaran, RP
Ozdol, VB
Ophus, C
et al.

Publication Date
2018-06-01

DOI
10.1016/j.actamat.2018.03.048

Peer reviewed

Multiscale Analysis of Nanoindentation-Induced Defect Structures in Gum Metal

R. P. Sankaran[a,*], V. B. Ozdol[b], C. Ophus[b], J. Kacher[b], C. Gammer[c], S. Govindjee[d], A. M. Minor[a,b] and J. W. Morris, Jr.[a]

[a]*Department of Materials Science and Engineering*, [d]*Department of Civil and Environmental Engineering*, *University of California*, *Berkeley*, *CA 94720*

[b]*National Center for Electron Microscopy*, *Molecular Foundry*, *Lawrence Berkeley National Laboratory*, *Berkeley*, *CA 94720*

[c]*Erich Schmid Institute of Materials Science*, *Austrian Academy of Sciences*, *Leoben*, *Austria*

Abstract

Using *ex-situ* transmission electron microscopy and the recently developed nanoprobe diffraction (NPD) technique, we characterize a nanoindented solution treated gum metal. Lattice rotations are resolved at a 1.2 nanometer length-scale and shown to be continuous within the nanoindentation pit; further, it is shown that these can be accommodated by a reasonable number of geometrically necessary dislocations at a density of ~10^15/m². We additionally provide direct evidence that dislocations within the nanoindent, rather than secondary phase nanoparticles, can serve as potent barriers to dislocation motion. We also demonstrate that plasticity in these alloys under nanoindentation can be accommodated solely by dislocation nucleation and propagation, with no competing deformation mechanisms present. Conventional transmission electron microscopy and "**g•b**" analysis reveal the presence of dislocations on <-111>{110} slip systems and highly localized plastic deformation in the form of shear bands on <111>{-1-12} slip systems, similar to previously observed "giant faults".

Keyword

gum metals; metastable beta-titanium alloys; nanoindentation; nanoprobe diffraction (NPD, or nanobeam electron diffraction, NBED); strain mapping

1. Introduction

Beta (β) (BCC) Ti-Nb alloys are attractive for bioimplants because of their low elastic moduli, biocompatibility, superelasticity, and shape-memory behavior [1,2,3]. A subset of these alloys termed "gum metals", developed by Toyota R&D [4], possess a low shear modulus in the $< 111 >_{\beta}$ direction and high yield strength. They also exhibit unusual mechanical behavior and defect structures, especially when tested after severe cold working. In the original investigations, their shear strength seemed to approach the ideal value at elastic instability ($0.11G_{<111>}$) [5], given the calculated elastic constants available at the time [6, 7]. The purported deformation structures supported the notion of ideal shear operating via giant fault formation and atomic–scale "nanodisturbances" [4,8,9].

Further research on this interesting material has revealed the complexity of its behavior in both the cold-worked and solution-treated conditions. Its possible deformation modes have been shown to include not only "giant faults", but ordinary dislocation flow [10, 11, 12, 13], deformation twinning [14, 15, 16], and transformation-induced plasticity via several different product phases [14,15,16], including possible transient phases that grow and shrink with the applied load [10, 16, 17]. As work on single-crystal variants has shown, both the mechanical response and the dominant deformation mechanism change with the sign and orientation of the applied stress [18, 19]. Both the phases that are present and the deformation behavior are also sensitive to minor changes in composition, as is typical of beta-Ti alloys. Given that this alloy was intentionally designed to reside at the limit of stability of the BCC phase, this complex behavior is not surprising, but it does emphasize the need for careful experimentation and characterization if the various aspects of its behavior are to be well understood.

One mechanical test that has proven useful in clarifying the fundamentals of mechanical behavior in recent years is nanoindentation, particularly when coupled with high-resolution characterization studies. A nanoindenter tests material that is ordinarily defect-free and imposes its maximum stress slightly beneath the contacted surface so that surface effects should not dominate the initiation of deformation [20]; there is strong evidence that nanoindentation can produce deformation at or very close to ideal strength [21], allowing the deformation modes that are activated to be studied in detail.

Prior work in this laboratory specifically included nanoindentation experiments on gum metal (solution-treated), coupled with high-resolution TEM studies of the deformation near the indentation pits [22]. Those studies produced a number of useful observations, but also identified three puzzling features of the deformation pattern that needed to be clarified. First, while a dense distribution of mobile dislocations was identified in the periphery of the pits, the centers of the pits appeared to be featureless, with no dislocations resolved. This suggests that some other mechanism might be operative. Second, the material within these featureless regions exhibited apparently continuous lattice rotations as the center of the pit was approached. Since local lattice rotations are ordinarily stabilized by crystal defects, this observation raised a serious question of what these defects might be. Third, the dislocations in the periphery of the pits were severely bowed, showing themselves to be strongly pinned by local obstacles. The nature of these obstacles could not be determined, raising the question of whether they are inherent features of the alloy, such as nano-precipitates, that might play an important role in its strengthening.

The present study aims to understand the observed behavior using *ex-situ* transmission electron microscopy (TEM) of solution treated gum metal (STGM) after nanoindentation.

Cross-sections of nanoindented STGM are analyzed via conventional TEM and annular dark field (ADF) imaging to give a more complete picture of the dislocation structure beneath the indent. Nanoprobe diffraction (NPD) is used to determine the exact nature of the sustained rotations and strain near the indent pit and to determine whether any secondary phases are mechanically induced. As we shall show, these more probative characterization techniques reveal a complex distribution of previously undetected dislocations that can fully account for the deformation field of the indentation pit. To our knowledge, ours is the first fundamental and detailed study of its kind to comprehensively analyze the defect structures that occur in a BCC material under nanoindentation, and the results and observations could potentially be more broadly applicable to BCC metals.

2. Materials and Methods

2.1. Sample preparation procedure

Material used in this investigation was supplied by Toyota Central R&D Laboratories, Nagakute, Japan as round bars of STGM with a nominal composition of 73.1Ti-23Nb-0.7Ta-2Zr-1.2O at.% These were fabricated by cold-isostatic pressing of elemental powders, sintering at 1300°C, hot forging at 1150°C, and solution-treating in Ar at 900°C [4]. Severe cold work of 90% was imparted by rotary swaging at room temperature (CWGM) followed by solution-treating in air for 30 minutes at 900°C (STGM). The STGM bars were cut perpendicular to the swaging direction into discs ~300 μm thick, disc cut to 3mm diameter, mechanically polished to ~100 μm thickness with SiC paper and jet polished on one surface in a Fischione Model 1010 twin-jet using an electrolyte solution of 4 vol% perchloric acid, 25 vol% butanol, and 71 vol% methanol at -30°C and 42V for 2min. Electropolishing provides a smoother, damage-free surface than mechanical polishing can, enabling acquisition of more reliable nanoindentation data. As

jet polishing results in a slight dimpling of the sample, only one side of the specimen was polished. The other side, covered with non-adhesive Teflon® tape to prevent polishing, retained a completely flat base for mounting on the nanoindentation stage. The electropolished side underwent nanoindentation *ex-situ* in a Hysitron Triboindenter® fitted with a diamond Berkovich tip. A triangular load-control function with 25mN maximum load and a loading/unloading rate of 5mN/s was used. The resulting load-displacement curves are similar to those in [22], in which no "pop-in" events are observed. Figure 1(top), schematically shows the sample set-up, where the indentation axis is nominally parallel to the swaging axis $< 110 >_{\beta}$.

The cross-section of one of the indents was prepared for TEM observation through the "*in-situ* lift-out technique" [23] using an FEI Strata dual beam SEM/FIB with Ga+ ion source equipped with an Omniprobe micromanipulator. The indent was first coated with a 2μm thick protective film of Pt and thinned to an initial thickness of 200nm at 30kV. An SEM image of the thinned lamella prior to lift-out is given in Figure 1(bottom). After the lamella was attached to the TEM grid, it was further milled and cleaned to a thickness of ~100nm at 6kV and 300pA.

2.2. Experimental facilities and parameters

Conventional TEM was performed on a JEOL 3010 microscope at 300 kV. ADF-STEM imaging was performed on an FEI Titan with a CEOS probe aberration corrector at 300 kV with 0.5Å probe size and 17.2mrad convergence semi-angle. ADF signal was collected at an inner collection semi-angle range of 24-35mrad. Scanning Nanoprobe Diffraction (NPD) was performed on an FEI Titan operating at 300kV in STEM mode. During High-Angular Dark Field HAADF imaging, a diffraction pattern was acquired for every probe position. The three independent condenser lenses enable STEM imaging with various convergence semi-angles. A sub-nm electron probe with a convergence semi-angle of ~0.9-1 mrad was used in nanoprobe

mode, yielding diffraction patterns with non-overlapping spots while enabling good spatial resolution (<1nm). Full diffraction patterns with 1024x1024 pixels resolution were captured relatively rapidly (0.1s) with the Gatan Orius 830 diffraction camera and custom software implemented in DigitalMicrograph.

2.3. Nanoprobe diffraction analysis algorithm

Diffraction patterns were analyzed offline using custom MATLAB code. Peak positions were located using a cross-correlation routine. High-pass filtering was performed prior to this step to remove the internal structure of diffraction disks. A pure cross-correlation method with filtering was optimal due to the thickness of the sample [24]. A peak-fitting algorithm was used on the original diffraction pattern to refine the initial peak position determined from the cross-correlation routine. Strain and rotation maps were then computed by calculating basis vectors for each pattern via a least squares approach. The deformation gradient tensor, $\boldsymbol{A}$, was computed with respect to a reference lattice, which was determined by calculating the median basis vectors from all the diffraction patterns included in the bottom half of the data set presented in Figure 6a. Thus, the color indices which we present are deviations of rotation and strain from this nominally deformation-free part of the sample. The deformation gradient was decomposed into stretch and rotation matrices via the singular value decomposition algorithm [25] such that $\boldsymbol{A} = \boldsymbol{UH}$, where $\boldsymbol{U}$ and $\boldsymbol{H}$ are rotation and stretch matrices, respectively. The rotation value, θ, was computed from the rotation matrix, since $\boldsymbol{U} = \begin{bmatrix} \cos\theta & -\sin\theta \\ \sin\theta & \cos\theta \end{bmatrix}$. We used the (Lagrangian) Biot strain measure $\boldsymbol{E} = \boldsymbol{H} - \boldsymbol{1}$. If the strain matrix is computed this way directly from the change in reciprocal lattice basis vectors, the strain components would represent the strains in reciprocal space. Since the measured lattice basis vectors were determined from the diffraction patterns, the real space strains were computed with $\boldsymbol{E}_{\boldsymbol{real\ space}} = \boldsymbol{1} - \boldsymbol{H}$.

3. Results

3.1. Nanoindentation data and analysis of defect structures

The load displacement curves obtained from nanoindentation, shown in Figure 2, are similar to those presented in [22], in which no "pop-in" events are observed. Using procedure indicated in Oliver and Pharr [26], mean hardness is calculated as 2.63GPa with a standard deviation of 0.06GPa. This value is consistent with previous hardness measurement of 250Hv (~ 2.45GPa) for both STGMs and CWGMs obtained by Saito et al. [27].

Immediately from Figures 3a and b, we observe that the nanoindentation process produces a large number of dislocations along with other defect structures such as shear bands and small angle grain boundaries. The clearly distinguishable dislocations 1-5 μm away from the pit appear as relatively long and discrete line defects, whereas the defects within the region immediately adjacent to the pit are not as easily observed or understood. This observation is at first consistent with the results of Withey et al. [22], particularly the supposed lack of dislocations observed in the indent pit. To understand the complex defect structure generated within the nanoindent, we perform (1) conventional "**g•b**" analysis on the discrete dislocations and shear bands further away from the indent pit, (2) ADF imaging to determine the origin of bowing and kinking observed in many of the dislocations and (3) NPD to quantify the large rotations and strains immediately adjacent to the indent pit.

3.1.1. Dislocation analysis: Burgers and line vector determination

Gum metals, having a BCC crystal structure, are likely to have dislocations with Burgers vector, **b**, of <111>-type. TEM images taken under a two-beam condition with the **g** = (200) reflection should render all dislocations of this type visible. Thus, in Figures 3c and 3d we present TEM images taken with both the **g=**(200) and **g**=(110) reflections, respectively, to

observe a majority of the dislocations generated within the sample. Of the easily distinguishable dislocations about the nanoindent, the discrete ones appear to be broadly divided into four configurations. Example dislocations within these four groupings are outlined in Figure 3c and d: the ones indicated in blue are referred to as horizontal, denoted by "H"; magenta as vertical, "V"; red as "Slant Up" and "Slant Down", "SU/SD"; and those within the yellow as Shear Band, "SB". The V- and H-type appear on both sides of the plastic zone, and the SU and SD types lie near the middle. We performed extensive "**g•b**" analysis and a coarse line trace analysis to determine the Burgers vectors and sense vectors of these dislocations groups. Details of this analysis are given in Supplementary Materials for each configuration, and the results are presented in Table 1. For the H and SU/SD groups, there is some ambiguity in determining the exact slip system. But, taking the data overall, we find that the observed discrete dislocations beneath the indent are consistent with slip systems typically found in BCC materials. Specifically, the two groupings, H and SU/SD, are comprised of dislocations consistent with the <-111>{110} slip system; the V-type of screw dislocations with **b** of <111>-type; and the SB dislocations in the shear bands reside on the <111>{-1-12}-type slip system. There may be other clearly distinguishable dislocations not belonging to these groups, but the majority of the dislocations further from the pit reside on the slip systems stated. Lastly, the presence of such dislocation configurations clearly demonstrates that the defect structure generated from nanoindentation has a certain order and structure.

3.1.2. ADF STEM imaging: dislocation-dislocation interactions

We next characterize the structures beneath the indent using lower magnification ADF and atomic resolution STEM imaging to further elucidate the nature of pinning points found in this study (Supplementary Materials) and previous studies [22, 12]. Due to enhanced diffraction and

strain contrast, ADF imaging conditions greatly aid in visualizing dislocations, enabling a better qualitative understanding of their true density and interactions.

ADF images of the regions underneath the nanoindent at various magnifications are presented in Figure 4, where we notice the dislocations appear white under dark field conditions. The observed dislocation arrangement is consistent with our previous results obtained from conventional TEM imaging. We notice again that a very large dislocation density is sustained within the deformed region beneath the indent, and, from Figure 4a, we determine that while there are no easily distinguishable defects immediately adjacent to the pit, we can clearly recognize the previously observed dislocation groups (H, V, SU/SD, SB) further away from the indent impression. Additional dislocations, not encompassed in these groups, are also present, but are difficult to discern due to the large amount of dislocation entanglement clearly observed in Figures 4b-d. Interestingly, within the bottom shear band in Figure 4d, we observe a dislocation cell network (DCN) within the band has formed. In the one above it, the band appears to be in an initial stage of DCN formation with heavily bowed dislocations with one overlapping segment.

To understand the cause of this severe dislocation bowing, we focus our attention on the boundary of the plastic zone. It is in these regions, just at the border between the deformed and the nominally un-deformed regions, that we find the dislocation density is significantly lower allowing for a clearer view of any dislocation interactions. Specifically, the area imaged in Figure 4c contains a region of lower dislocation density next to the indent impression. We observe a particular dislocation situated ~150-200 nm away from the high-density zone which is outlined in Figure 5a. A higher resolution ADF image of this dislocation is presented in Figure 5b, in which it appears heavily bowed with a defect structure/pinning point ahead of its cusp.

Increasing the resolution further, we present an atomic resolution image in Figure 5c. The pinning point appears as a linear defect with a complex atomic motif, in which extra atomic columns appear between the BCC column locations (where the BCC-Ti matrix is oriented nominally along [001] zone axis.) A model of the superlattice motif (green) is superimposed on the BCC matrix (red) in Figure 5d. In the model, it is apparent the superlattice is best described as helicoidal atomic displacements about the core of a mixed dislocation [28, 29]. Here, the mixed dislocation is ~20 atomic columns wide (~4.5nm) with an observed length of ~7nm. The Burgers vector, **b,** of the dislocation appears to lie along the [110] direction. As the ADF image is a projection down the nominal [001] zone axis, the [-1-11] and [-1-1-1] directions in projection coincide with the [110] direction. Thus, we determine **b** of the dislocation to be consistent with a/2<111>-type, supporting the result from the "**g•b**" analysis in Section 3.1.1. The sense of the dislocation, **u,** appears to lie along the projected [00-2] direction, but cannot be exactly determined from one image. We conclude the bowing of the original dislocation is due to elastic interaction with this mixed dislocation.

3.1.3. Nanoprobe diffraction (NPD): continuous lattice rotations in STGM

To complete our analysis, we examine regions closer to the indent, where higher stresses are endured. As previously mentioned, ADF and conventional TEM imaging indicate that the dislocations adjacent to the indent pit are too dense to be easily observed singularly or discretely (Figure 4a, Figure 3a and 3b). Withey et al. [22] provided some evidence indicating that STGMs exhibit a continuous rotation about specific axes within the nanoindentation pit. To better understand the deformation behaviors and quantify the observed lattice rotations, we provide rotation and strain maps calculated from the NPD data in Figures 6-8 measured from different regions of the nanoindent. The foil normal is very close to the [001] zone, and we tilted to this

axis for acquiring all diffraction patterns. The x and y directions for the strain component calculation are defined to be in the [-1-10] and [1-10] directions, respectively, of the reference lattice (consistent with the indexing of the diffraction pattern in Supplementary Fig. 3). We note here that the resultant rotation and strain maps obtained from the NPD technique given in Figures 6-8 show outliers, noisy edges, and, in some cases, horizontal "streaking". Horizontal streaks are due to the Titan PC pausing during data acquisition and the noisy edges occur at the end of the scanning line. Thus, the calculated rotation and strain maps presented are largely raw and unfiltered.

We define **w** as the probe scanning direction and **v** as the direction the probe moves to start the next row. For the data presented in Figure 6, we used a ~40 nm step size for both **w** and **v** with 128x128 probe positions. From Figure 6a, we notice that only regions closest to the indentation impression have sustained large in-plane lattice rotations, and these regions appear to be divided into four zones, with each one of opposite sense to the adjacent zone. We find no large rotation–free areas directly adjacent to the nanoindent impression, as was found in the previous studies [30, 31]. A significant rotation difference, about 26° in-plane, is measured on the left side of the indent impression between the two left rotational lobes.

The in-plane strain maps in Figure 6b show large sustained strains within the sample, up to +/- 8% in local regions. We observe large regions of positive strain (dilatation) in $\varepsilon_{xx}/\varepsilon_{yy}$ (yellow/red) that extend out from the indent and also regions of negative strain in $\varepsilon_{xx}/\varepsilon_{yy}$ (blue/light blue) near the indent tip. In general, these regions of tensile and compressive strain correlate well with the bright and dark diffraction contrast, respectively, shown in the ADF

image of the indent (Figure 4a).[1] The largest compressive strains occur directly beneath the indenter tip as expected, which are indicated by dark blue zones in the ε_{xx} and ε_{yy} maps. This region adjacent to the indenter tip also sustains the largest shear strains as well, indicated by the adjacent blue and red zones in the ε_{xy} map.

Within the shear bands, we find the material has also sustained large strains. The arrows in the $\varepsilon_{xx}/\varepsilon_{yy}$ maps in Figure 6b indicate diagonal bands of compressive and tensile strains that demarcate the positions of the bottom three shear bands (refer to Figure 3c). The regions in between these shear bands are nominally free of strain, as expected, except we find in the ε_{xx} map a large region sustaining ~3% compressive strain between the bottom two shear bands. This region appears to be nominally dislocation free as evidenced by the lack of contrast in the ADF image of Figure 4a. For this sample, we assume the origin of strain to be mainly due to the overlap of the strain fields of the generated dislocations, and that any residual elastic strain would have relaxed during TEM sample preparation. There are a couple of possibilities that could explain this feature. It is possible some residual compressive strain may have been locked in due to oxide growth during sample preparation or from the deposition of the protective platinum layer as either constraint could impede full relaxation of the foil. There may also be some out-of-plane rotation in this region. It is conceivable that the generated internal defect structure itself in this region may be responsible for out-of-plane tilt. Such tilting or bending may change the strain and rotation decomposition such that strain appears to be present here. This could be true throughout the sample (although we checked that any out-of-plane tilt was

[1] In keeping with common usage, we refer to positive and negative normal strains as tensile and compressive, respectively, with the full knowledge of the imprecision of such terminology when discussing systems with residual stresses.

reasonably low), and so the actual strain values given in the maps should not be considered absolute as they may be larger than actual.

To aid in physically interpreting the measured strains, we can calculate an equivalent deviatoric (Biot) strain directly from the 2x2 stretch matrix $\boldsymbol{H}$ as follows. A 3x3 stretch matrix $\boldsymbol{H}$ is constructed, where the off-diagonal, out of plane components are assumed to be zero and the zz-diagonal component is taken to be the inverse of the determinant of the 2x2 $\boldsymbol{H}$ matrix, i.e. incompressible plastic flow. The 3x3 strain matrix, $\boldsymbol{E}$, is computed from $\boldsymbol{H}$, and finally we take the norm of this finite strain deviatoric matrix and multiply by $\sqrt{2/3}$. The result, given in Figure 6c, can be interpreted as an equivalent deviatoric (Biot) strain measure using an assumption of incompressibility. This metric should approximate the actual shear strain endured by the sample. This equivalent strain appears physically reasonable through most of the indent and rises steeply in the region directly underneath the indentation apex, as expected. This map thus physically substantiates the measured diffraction data and resultant strain and rotation calculations.

As we are also interested in the continuous lattice rotations beneath the indent, we performed NPD experiments at higher spatial resolutions about the two rotational lobes observed on the left side of the indent, outlined in red in Figure 7a. For the maps in Figure 7, we used a step size in **w** and **v** of ~40nm with 32x32 probe positions. The rotation map measured from the data is shown in Figure 7b (the indent has been rotated in the image, such that its left boundary lies horizontally).

A bright-field TEM image of one of the lobes, along with its boundary, is shown in Figure 7 and is a higher magnification image of the region outlined in blue in Figure 7a. We observe a dense forest of dislocations is present adjacent to the indent within this lobe and conclude that these dislocations must be responsible for the measured lattice rotations. Due to the constantly

changing orientation in this part of the sample, the images (both Figure 7a and c) do contain regions in which there are no immediately visible dislocations. Upon specimen tilting, however, we confirm that forest configurations are present in all areas adjacent to the indent impression. Thus, there is strong evidence suggesting that typical dislocations may be responsible for the measured continuous lattice rotations.

From the given in-plane rotation map (Figure 7b), we can directly quantify the density of geometrically necessary dislocations required to sustain the measured lattice rotations by computing Nye's dislocation tensor. Tensor components were computed using a custom Matlab script based on the derivation by Pantleon (2008), in which the analysis was applied to similar rotation data acquired from EBSD [32]. For the calculation, we used a Burgers vector of $2.85*10^{-9}$m$*a_0/2*<111>$. Figure 7d gives the α_{xz} and α_{yz} components, where the basis vectors **x**, **y**, and **z** are nominally parallel to the [-1-10], [1-10] and [001] directions, respectively, consistent with the previous data sets shown. From the dislocation maps, we find the densities associated with the boundary between the lobes, where the rotation gradient is largest, are ~ $10^{15}/m^2$ for both α_{xz} and α_{yz}. The calculated GND, while large, is not unreasonable for a heavily deformed material and indicates that the measured rotations displayed in Figure 7b is physically plausible.

To further investigate the nature of this large rotation gradient on the side of the indent (Figure 7b), we performed NPD at an even higher spatial resolution. For the maps in Figure 8a and b, we used a ~1nm probe size and 6.7 x13.4nm step size in **w** and **v** with 128x32 probe positions. Such resolution will allow us to determine whether the boundary between the rotational lobes is comprised of a discrete, small-angle grain boundary or the rotations are truly continuous at the nanometer scale. The resulting rotation map is given in Figure 8a and is superimposed upon the HAADF image of the indent. At the reduced step size used, the lattice

rotations appear mostly continuous except right at the junction between the lobe and indent boundary (yellow). Here, the change in rotation sense appears discrete, in that it changes substantially over a couple of nm. This boundary region between the rotational lobes was further analyzed with 128x128 probe positions at a step size in **w** and **v** of 1.2 nm. The resulting rotational map is given in the Figure 8a inset. Interestingly, the boundary between the adjacent lobes appears discrete on the upper right near the nanoindent boundary, jumping from 3° to -6° within a couple of nm. Such a large, discrete rotational jump, ~9°, indicates possible low-angle grain boundary formation. However, this discrete interface quickly becomes more diffuse away from the indentation boundary. Thus, it appears that the boundary between these lobes of opposite rotational sense are largely continuous in nature at the nm scale.

The corresponding strain maps associated with this data set are given in Figure 8b, which use the same x-y coordinate system defined in Figure 6b. In general, there are positive tensile strains of ~ 2-3% in both the x and y directions throughout the region. Further, it appears that larger strains (~ 6-9%) are endured on the right side of the ε_{xx} map and on the left side of the ε_{yy} map. The division between the areas of smaller and larger strains appears on the diagonal of the map, correlated with the position of the rotational lobe boundary. The ε_{xy}, map reveals that only a negligible amount of shear strain is present in this region.

4. Discussion

The three intriguing aspects of the deformation of STGM under nanoindentation that motivate this study involve understanding the defect structure within the seemingly featureless nanoindentation pit, the exact nature of the continuous rotations comprising this region, and the severe dislocation bowing surrounding the indent pit that indicated the presence of structural obstacles. With respect to the questions regarding the indentation pit, we have been able to

quantify the lattice rotations and find a physically reasonable dislocation density that may be accommodated. Correlative bright field TEM imaging confirms the presence of very dense, complex dislocation structures likely mediating these rotations. We also find that dislocations outside the indent pit, while remaining elusive to directly image or observe, particularly if small or oriented unfavorably, can serve as potent barriers to the motion of other dislocations. Previous studies have observed dislocation motion being hindered, both directly [12] and indirectly [4], and it has been speculated that atomic-scale embryos of ω phase or ZrO clusters could be responsible. Here we argue that dislocations themselves may very well have been effective obstacles in these cases.

In pursuing this in-depth investigation, additional intriguing observations emerged involving specific dislocation arrangements along with a lack of other intruding deformation mechanisms, shear banding, and the presence of rotational lobes in the pit. These features are also addressed in detail in the following sections.

4.1. Dislocation-mediated plasticity in STGMs

The main results from TEM imaging demonstrate that the deformation behavior of STGM under nanoindentation appears to be solely governed by a/2<111>-type dislocation glide on both the {110} and {112} plane families (Figure 3). We note that no secondary spots were observed in the raw diffraction data in this study. The observation of a plastic deformation mechanism involving only dislocation slip in gum metals is not typical. Of course, the original paper on gum metal by Saito et al [4] claimed a dislocation-free ideal shear deformation mechanism mediated by giant faults formed via nanodisturbance generation, which seemed to be supported by the results of mechanical testing in which gum metal exhibited a lack of work hardening [4, 27] and a tensile strength near its ideal value [4] given the measured elastic constants available at

the time [33,34].[2,[35,36]]. However, more recent studies of gum metals have typically observed a mix of dislocation slip, stress-induced phase transformations, and mechanical twinning upon deformation. Specifically, a combination of deformation induced ω or martensitic α'', twinning, and slip band formation have been observed in uniaxial tension [15], compression [14, 17], and in elastic load cycling of STGMs [16]. Yet, in each of these studies, dislocation slip either coexisted with these mechanisms or simply did not play a significant role, if any at all. Few other studies have claimed a sole dislocation slip-based plasticity mechanism [12, 13] for STGMs, as we do.

The remaining question in this study is, given that typical BCC twinning modes and stress-induced ω have been observed in as-received CWGM samples [37, 10] and upon deformation of STGMs [14, 15], "why we would fail to observe them here?" Firstly, it is well known that the operating deformation mechanism of Beta-Ti alloys is extremely sensitive to the stability of the beta phase [38, 39]. Beta-Ti stability can be empirically quantified by the Molybdenum equivalent (Mo_{eq} metric) [40], where the alloy is considered stable against martensitic transformation roughly above a Mo_{eq} value of 10. The gum metal used in the present study did not appear to contain any athermal ω (ω_{ath}) phase after solution treatment and final quench, consistent with its Mo_{eq} value of 10.49. In a uniaxial tension experiment of cast STGM by Plancher et al. [15] deformation-induced ω and <111> {112} twinning was observed, but the sample initially contained ω_{ath} upon quench implying an intrinsic beta-instability consistent with its lower Mo_{eq} value of 10.27. Similarly, Yang et al. [14] demonstrated under uniaxial compression that <111>{112}, <113>{ 332}twinning and deformation-induced ω coexisted with

[2] We note that a lack of work hardening in tensile curves is likely typical of many Ti alloys, especially β-Ti 27alloys [35], and that the ideal strength was later recalculated via experimentally determined elastic constants to be roughly double the tensile strength [36].

dislocation slip for their STGM, also consistent with its lower Mo_{eq} of 10.34. While these values may appear relatively close to that of the present alloy, the composition of gum metals has been specifically engineered to lie right on the edge of beta stability, and it seems reasonable that deviation of this parameter towards instability could drastically change the dominant deformation mechanism. Specifically, the mechanism of mechanical twinning and ω transformation is thought to be directly aided by structural instability of the BCC lattice. <111>{112} twinning can be realized through a/6<111> shear on successive {112} planes. Similarly, while the β -> ω transformation is typically easily understood through a shuffle mechanism involving the "collapse" of {111}-plane pairs, it may also be described by inhomogeneous shear in <111>-type directions on successive {112} planes [41]. The lower shear modulus in the <111> direction induced by decreased β-phase stability will lower the energy barrier for the shear required by either transformation. Further, the presence of any ω_{ath} could also lower the nucleation barrier for deformation-induced phase transformations compared to an alloy initially free of secondary phases. Consistent with this reasoning, Castany et al. [12] and Kamimura et al.[13] tested STGMs with a Mo_{eq} of 10.49 and 10.45, respectively, and observed direct and indirect evidence, respectively, of dislocation slip only. Some authors of the present study have in fact performed <110> nanoindentation on another specimen provided by Toyota Central R&D but leaner in Nb, with a lower Mo_{eq} of 9.37 and containing initial ω_{ath} precipitates. The results of this experiment yielded clear <111>{112}mechanical twins and stress-induced ω laths in direct contrast to the results in this investigation [42].

It is clear from these prior studies that other deformation mechanisms can intrude in other stress states apart from nanoindentation. We simply establish in this study that these mechanisms are not needed to explain behavior in nanoindentation, and dislocation slip can fully account for

defect structures observed here. Still, we are aware that the deformation patterns we have analyzed are those that exist post-indentation. It remains possible that other deformation modes intrude during the indentation itself, which evolve into dislocation configurations as the system relaxes after deformation. This seems unlikely, with the possible exception of the shear bands, since the dislocation patterns are obviously compatible with the overall deformation imposed by the indent.

4.2. On Giant Fault mechanism

Also found in this study were highly localized regions of plastic deformation occurring within shear bands on the <111>{-1-12} slip system (Figure 3b), some of which contained dislocation cell networks. These shear bands appeared as isolated regions surrounded by swaths of un-deformed material, very similar to the "giant fault" structures reported for deformed gum metals [4, 8]. In the present study, we found the shear bands lie on the {112}-type plane. Similarly, Kuramoto et al. [8] observed that the giant faults in STGMs after tensile testing also lied close to {112}-type planes, specifically rotated 13° away from [111] (1-1-2) about the [110] direction and oriented ~45° to the tensile axis. However, they did not observe any discrete dislocations within the faults, only local lattice rotations surrounding them. The orientation of the faults as 45° from the tensile axis without the presence of dislocation structures seemingly supported the theory that gum metals deform via ideal shear. Further, first principles calculations of elastic constants in gum metal approximants detailed how an applied shear oriented ~13° from <111>(1-1-2) about the [110] direction can allow, with help from a particular soft phonon mode in gum metals to aid atomic shuffle, for transformation to the HCP structure [43]. This structural transformation as a deformation mechanism could further explain the lack of dislocation evidence near the giant faults (although, no secondary phases were observed in the original

studies). In the present study, however, we have clear evidence that the motion of dislocations with **b** of <-111>-type is responsible for the shear bands observed on the {112} planes.

A few possibilities can explain the differences between our and prior studies with respect to giant faults and shear bands. First, it is possible that actual dislocations were present in the giant faults: the prior studies prepared samples to view faults along their traces, and in our study, we view the projection of the face of the shear band allowing clear visualization of the structures from which they are comprised. On the other hand, our study involved compression via nanoindentation, and it is possible that any ideal shearing mechanism may have been suppressed by surrounding material constraints, whereas in a tensile test, the giant faults could propagate easily through the material to free, unconstrained, surfaces. These free surfaces allow for the deformed material within the faults to protrude above the original surface, as clearly seen in images in Ref. [8].

4.3. Nanoindentation-induced lattice rotations

One of our original questions was whether the large lattice rotations, as observed qualitatively in nanoindented STGM [22], were continuous and could be accommodated by a reasonable quantity of dislocations. The dislocation density calculated from the NPD data linked with the dense forest of dislocations explains the origin of severe rotations, previously observed under nanoindentation, to be conventional slip (Figure 7c, d). In quantifying the rotation, we found rotational lobes of opposite sense adjacent to each other. Prior studies utilizing the EBSD technique have also observed large crystal reorientation zones as well. Table 2 presents a summary of these studies (Refs. [30, 31, 44, 45]) along with the current investigation. It is noted that there is no readily available prior study for BCC materials and comparison is made with FCC materials. Most authors observe multiple lobes and agree that lattice re-orientation near the

indent is likely due to slip. Most studies observe rotation free areas between the zones, whereas we find they are immediately adjacent to each other. Other features that we observe, including small-angle grain boundaries, are consistent with those found in previous studies. Our study is distinguished from previous ones in that we investigated a BCC metal using the TEM-NPD technique to demonstrate, for the first time, the truly continuous nature of these rotations at the nanoscale utilizing a step size of 1.2nm. While the continuous lattice rotations are not necessarily unique to gum metal, or BCC materials, perhaps the range, spatial extent and character of the rotational lobes may be. Our analysis further revealed that the dislocation and slip structures further from the indent had a specific arrangement. The observation of shear bands and the determination of the character of dislocations comprising them is also unique to this study.

5. Conclusions

Extensive characterization of a FIB lift-out cross section of a nanoindented STGM sample was performed. From conventional TEM analysis, including "**g•b"** analysis**,** ADF imaging, and the powerful nanoprobe diffraction technique, we conclude the following:

- The deformation in and around the indentation pit can be fully explained by the dense, complex distribution of dislocations that is revealed by these modern techniques. The only defects observed are dislocations groups on slip systems typical of BCC materials: <-111> {110} and <111>{-1-12}. No second-phase particles or twins appear, though there are regions of highly localized plastic deformation in which the dislocations are organized into shear bands on {112}-type planes that resemble the "giant faults" previously observed in tensile-loaded STGMs.

- Nanoprobe diffraction using steps sizes as small as 1.2nm shows that the lattice rotations found near the center of the pit in prior work are real and truly continuous. However, the pit centers are not devoid of defects. They contain a very high density of dislocations, which are, apparently, the "geometrically necessary dislocations" that produce the lattice rotation. The required dislocation density is near $10^{15}/m^2$, which is very high, but not unreasonable.
- The local obstacles that strongly pin mobile dislocations in the periphery of the pit are not nanoparticles, but are forest dislocations. Their crystallography is characterized and explained.
- The deformation accomplished by nanoindentation in solution treated gum metal is due to a dense distribution of dislocations that are normal in BCC metals. While this is the only detailed study known to us of deformation under nanoindentation in a BCC metal, it is entirely possible that the pattern observed here is typical of BCC metals.

6. Acknowledgments

Authors gratefully acknowledge helpful discussions with Thomas C. Pekin on various algorithms for disk position determination in nanoprobe diffraction data.

7. Funding

The authors acknowledge support of the National Science Foundation under Grant Nos. DMR-0706554, DMR-1105081 and Toyota Research and Development. All conventional TEM imaging, NPD STEM imaging and image processing was performed at the Molecular Foundry, supported by the Office of Science, Office of Basic Energy Sciences of the U.S. Department of Energy under Contract No. DE-AC02—05CH11231.

[1] P. Laheurte, F. Prima, A. Eberhardt, T. Gloriant, M. Wary, E. Patoor, Mechanical properties of low modulus beta titanium alloys designed from the electronic approach, J. Mech. Behav. Biomed. Mater. 3 (2010) 565-573.
[2] M. Niinomi, T. Hattori, K. Morikawa, T. Kasuga, A. Suzuki, H. Fukui and S. Niwa, Development of low rigidity β-type titanium alloy for biomedical applications, Mater. Trans. 43 (2002) 2970-2977.
[3] H. Y. Kim, H. Satoru, J.I. Kim, H. Hosoda and S. Miyazaki, Mechanical Properties and Shape Memory Behavior of Ti-Nb Alloys, Mater. Trans. 45 (2004) 2443-2448.
[4] T. Saito, T. Furuta, J.H. Hwang, S. Kuramoto, K. Nishino, N. Suzuki, R. Chen, A. Yamada, K. Ito, Y. Seno, T. Nonaka, H. Ikehata, N. Nagasako, C. Iwamoto, Y. Ikuhara and T. Sakuma, Multifunctional Alloys Obtained via a Dislocation-Free Plastic Deformation Mechanism, Science 300 (2003) 464-467.
[5] C.R. Krenn, D. Roundy, J.W. Morris Jr., M.L. Cohen, Ideal strengths of bcc metals, Mater. Sci. Eng. A 319–321 (2001) 111–114.
[6] T. Li, J. W. Morris, Jr., N. Nagasako, S. Kuramoto, D. C. Chrzan, ‘‘Ideal’’ Engineering Alloys PRL 98 105503 (2007).
[7] H. Ikehata, N. Nagasako, T. Furuta, A. Fukumoto, K. Miwa, T. Saito, First-principles calculations for development of low elastic modulus Ti alloys, PRB 70 **174113** (2004).
[8] S. Kuramoto, T. Furuta, J.H. Hwang, K. Nishino, and T. Saito, Plastic Deformation in a Multifunctional Ti-Nb-Ta-Zr-O Alloy, Met and Mat Trans A 37A (2006) 657-662.
[9] M.Y. Gutkin, T. Ishizaki, S. Kuramoto and I.A. Ovid’ko, Nanodisturbances in deformed Gum Metal, Acta Mater. 54 (2006) 2489-2499.
[10] R. J. Talling, R. J. Dashwood, M. Jackson, D. Dye, On the mechanism of superelasticity in Gum metal, Acta Mater. 57 (2009) 1188-1198.
[11] H. Xing, J. Sun, Q. Yao, W. Y. Guo, R. Chen, Origin of substantial plastic deformation in Gum Metals , APL 92 **151905** (2008).
[12] P. Castany, M. Besse, T. Gloriant, Dislocation mobility in gum metal β – titanium alloy studied via *in situ* transmission electron microscopy, PRB 84 **020201** (2011).
[13] Y. Kamimura, S. Katakura, K. Edagawa, S. Takeuchi, S. Kuramoto, T. Furuta, Basic Deformation Mechanism of BCC Titanium-Based Alloy of Gum Metal, Mat. Trans. 57 **9** (2016) 1526-1534.
[14] Y. Yang, S. Q. Wu, G. P. Li, Y. L. Li, Y. F. Lu, K. Yang, P. Ge, Evolution of deformation mechanisms of Ti–22.4Nb–0.73Ta–2Zr–1.34O alloy during straining, Acta Mater. 58 (2010) 2278-2787).
[15] E. Plancher, C. C. Tasan, S. Sandloebes, D. Raabe, On dislocation involvement in Ti-Nb gum metal plasticity, Scripta Mater. 68 (2013) 805-808.
[16] V. A. Vorontsov, N. G. Jones, K. M. Rahman, D. Dye, Superelastic load cycling of Gum Metal, Acta Mater. 88 (2015) 323-333.
[17] E. A. Withey, A. M. Minor, D. C. Chrzan, J. W. Morris Jr., S. Kuramoto, The deformation of Gum Metal through in situ compression of nanopillars, Acta Mater, 58 (2010) 2652-2665.
[18] J. W. Morris, Jr., Y. Hanlumyuang, M. Sherburne, E. Withey, D. C. Chrzan, S. Kuramoto, Y. Hayashi, M. Hara, Anomalous transformation-induced deformation in <110> textured Gum Metal, Acta Mater. 58 (2010) 3271-2380.
[19] N. Takesue, Y. Shimizu, T. Yano, M. Hara, S. Kuramoto, J. of Crystal Growth, 311 (2009) 3319-3324.

[20] A. M. Minor, S. A. Syed Asif, Z. Shan, E. A. Stach, E. Cyrankowski, T. Wyrobek, and O. L. Warren, A new view of the onset of plasticity during the nanoindentation of aluminium, Nature Materials, 5, (2006), 697-702.
[21] "Springer Handbook of Experimental Solid Mechanics," W. N. Sharpe Editor, Springer US (2008).
[22] E. Withey, M. Jin, A. Minor, S. Kuramoto, D.C. Chrzan and J.W. Morris, Jr., The deformation of "Gum Metal" in nanoindentation, Mat. Sci Eng. A 493 (2008) 26-42.
[23] J. Mayer, L. A. Giannuzzi, T. Kamino and J. Michael, TEM Sample Preparation and FIB-Induced Damage, MRS Bulletin 32 (2007) 400-407.
[24] T. C. Pekin, C. Gammer, J. Ciston, A. M. Minor. C. Ophus, Optimizing disk registration algorithms for nanobeam electron diffraction strain mapping, Ultramicroscopy 176 (2017) 170-176.
[25] N. J. Higham, Computing the polar decomposition---with applications, SIAM J. Sci. Stat. Comput., 7(4), 1986, 1164-1174.
[26] W. C. Oliver and G. M. Pharr, An improved technique for determining hardness and elastic modulus using load and displacement sensing indentation experiments, J. Mater. Res, 7 No. 6 (1992) 1564-1583.
[27] T. Saito, T. Furuta, J.H. Hwang, S. Kuramoto, K. Nishino, N. Suzuki, R. Chen, A. Yamada, K. Ito, Y. Seno, T. Nonaka, H. Ikehata, N. Nagasako, C. Iwamoto, Y. Ikuhara and T. Sakuma, Mater. Sci. Forums**,** Multifunctional Titanium Alloy "Gum Metal", 426-424 (2003) 681-688.
[28] D. Hernandez-Maldonado, H. Yang, L. Jones, R. Groger, P. B. Hirsch, Q. M. Ramasse, P. D. Nellist, STEM optical sectioning for imaging screw dislocation core structures, The 16th European Microscopy Congress (2016).
[29] C. Chen, C. Zhu, E. R. White, C. Chiu, M. C. Scott, B. C. Regan, L. D. Marks, Y. Huang, J. Miao, Three-dimensional imaging of dislocations in a nanoparticle at atomic resolution Nature, 496 (2013) 74-77.
[30] N. Zaafarani, D. Raabe, F. Roters, S. Zaefferer, On the origin of deformation-induced rotation patterns below nanoindents, Acta Mater. **56** (2008) 31-42.
[31] J. W. Kysar, Y. X. Gan, T. L. Morse, X. Chen, M. E. Jones, High strain gradient plasticity associated with wedge indentation into face-centered cubic single crystals: Geometrically necessary dislocation densities, J. Mech. Phys. Solids (2007) 1554-1573.
[32] W. Pantleon, Resolving the geometrically necessary dislocation content by conventional electron backscattering diffraction, Scripta Mater. 58 (2008) p. 994–997.
[33] T. Li, J. W. Morris, Jr., N. Nagasako, S. Kuramoto, D. C. Chrzan, ''Ideal'' Engineering Alloys PRL 98 105503 (2007).
[34] H. Ikehata, N. Nagasako, T. Furuta, A. Fukumoto, K. Miwa, T. Saito, First-principles calculations for development of low elastic modulus Ti alloys, PRB 70 **174113** (2004).
[35] "ASM Atlas of Stress-Strain Curves", ASM International, Materials Park, OH (2002).
[36] R.J. Talling, R.J. Dashwood, M. Jackson, S. Kuramoto, D. Dye, Determination of (C_{11} - C_{12}) in Ti–36Nb–2Ta–3Zr–0.3O (wt.%) (Gum metal), Scripta Mater. 59 (2008) 669-672.
[37] T. Yano, Y. Murakami, D. Shindo, S. Kuramoto, Study of the nanostructure of Gum Metal using energy-filtered transmission electron microscopy, Acta Mater. **57** (2009) 628-633.
[38] S. Hanada, O. Izumi, Transmission Electron Microscopic Observations of Mechanical Twinning in Metastable Beta Titanium Alloys, Met. Trans. A. **17A** (1986), p. 1409.

[39] S. Ankem, C.A. Greene, Recent developments in microstructure:property relationships of beta titanium alloys, Materials Science and Engineering A **263** (1999) p.127–131.
[40] P.J. Bania, Beta Titanium Alloys and Their Role in the Titanium Industry JOM, 46, 16 (1994).
[41] L. M. Hsiung and D. H. Lassila, Shock induced Deformation Twinning and Omega Transformation in Tantalum and Tantalum-Tungsten Alloys, Acta Mater **48** (2000).
[42] R. P. Sankaran, Deformation Mechanisms of Gum Metals Under Nanoindentation, University of California, Berkeley (2015).
[43] Y. Hanlumyuang, R. P. Sankaran, M. P. Sherburne, J. W. Morris Jr., D. C. Chrzan, Phonons and phase stability in Ti-V approximants to gum metal, PRB 85 144108 (2012).
[44] S. J. Lloyd, A. Castellero, F. Giuliani, Y. Long, K. K. McLaughlin, J. M. Molina-Aldareguia, N. A. Stelmashenko, L. J. Vandeperre and W. J. Clegg. Observations of nanoindents via cross-sectional transmission electron microscopy: a survey of deformation mechanisms, Proc. R. Soc. A 461 (2005) 2521-2543.
[45] M. Rester, C. Motz, R. Pippan, Microstructural investigation of the volume beneath nanoindentations in copper, Acta Mater. 55 (2007) 6427–6435.

Figure 1: Schematic of ex-situ lift-out for TEM observation of nanoindentation in cross section (XS) is provided. (Top) Gum metal cut perpendicular to the swaging axis, which has developed <110> texture. Nanoindent ROI retrieved via lift-out within dotted rectangle. (Bottom) SEM image of sample lamella prior to lift-out and final cleaning.

Figure 2: Nanoindentation load-displacement curves for STGM sample. Reduced modulus, Er, of 91GPa and hardness of 2.63GPa was calculated. No obvious pop-ins observed.

Figure 3: Overview bright field TEM images of the nanoindentation cross section. Figures 3a and 3b are taken at different sample tilts. A variety of defect structures are observed, including dislocations and small angle grain boundaries (red dotted lines). Highly localized plastic deformation occurs in shear bands (red arrows). Figures 3c and 3d are images taken with the given two-beam condition, and four main dislocation groups are present. Example dislocations from each group outlined: horizontal, “H” (blue), vertical “V” (magenta), Slant up and Slant Down “SU+SD” (red), and shear bands “SB” (yellow boxes).

Figure 4: ADF images of the nanoindent. a) Large density of dislocations and defects are observed, and the shear bands and dislocation groups previously discussed are apparent. b-d) Higher magnification images of regions about the indent: b) upper left, c) upper right, and d) central portion of the indentation area show complex dislocation interactions and entanglement.

Figure 5 a) Higher magnification ADF image of the region in Figure 5c, with bowing dislocation circled b) A defect (arrow) is observed ahead of the cusp of the bowed dislocation. c). Atomic resolution of this linear defect contains superlattice peaks in between BCC matrix columns. d) Model of atomic motif within the linear defect, where red is BCC matrix and green denotes the extra atomic columns. Model shows helicoidal atomic displacements present around a dislocation core. Linear defect that causes bowing is determined to be mixed dislocation with b= a/2 [-1-11], indicating strong, elastic dislocation-dislocation interactions within nanoindent.

Figure 6: Nanoprobe diffraction results are given for overview of indent, taken with 128x128 probe positions at a ~40nm step. a) Rotation map is presented, where theta sense is about z-axis, parallel to [001] direction of reference lattice. Map reveals four rotational lobes of opposite sense to the adjacent lobe in the immediate vicinity of indent. b) Strain maps with reference axes given show tensile strains of up to +/-8%. Largest compressive strains occur beneath the indentation apex. Shear bands have also sustained large strains (arrows). c) An equivalent deviatoric (Biot) strain measure for the entire indent was calculated and is largest directly beneath the indentation tip.

Figure 7: a) Nanoprobe diffraction was performed within red ROI using 32x32 probe positions and ~40nm step size. b) Resultant in-plane rotation map shows continuous rotation of ~26° is sustained near the indent. c) TEM image of the boundary between the two left-most rotational lobes (blue ROI in a) contains high dislocation density. d) α_{xz} and α_{yz} elements of Nye's dislocation tensor computed from the in-plane rotation map in b) give GND of up to ~10^15/m2.

Figure 8 a) Rotation map was acquired with 128x32probe positions at 6.7nmx13.4nm step size. (Inset) Region containing boundary was mapped at 128x128 probe positions, 1.2nm step size. Possible small angle grain boundary is forming adjacent to the indent. Boundary becomes diffuse away from the indent revealing continuous nature of rotations at the nm-scale. b) Strain maps show positive tensile strains are present in the region.

Table 1: Results from conventional "g•b" analysis of the main observed dislocation groups.

Table 2: Experimental parameters and results from previous indentation investigations, along with the present study, are summarized. Observation of counter-rotational lobes adjacent to the indent is consistent between all studies. The present study is distinguished from prior studies in utilizing the NPD technique with small (1.2nm) step size to investigate a BCC material.

*Figure(s) 1

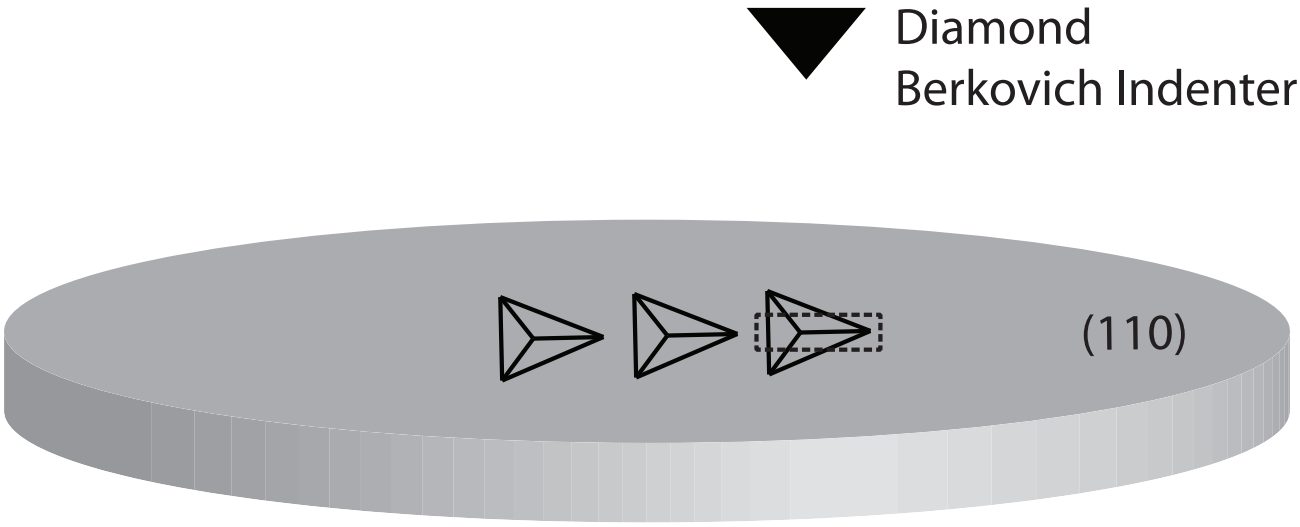

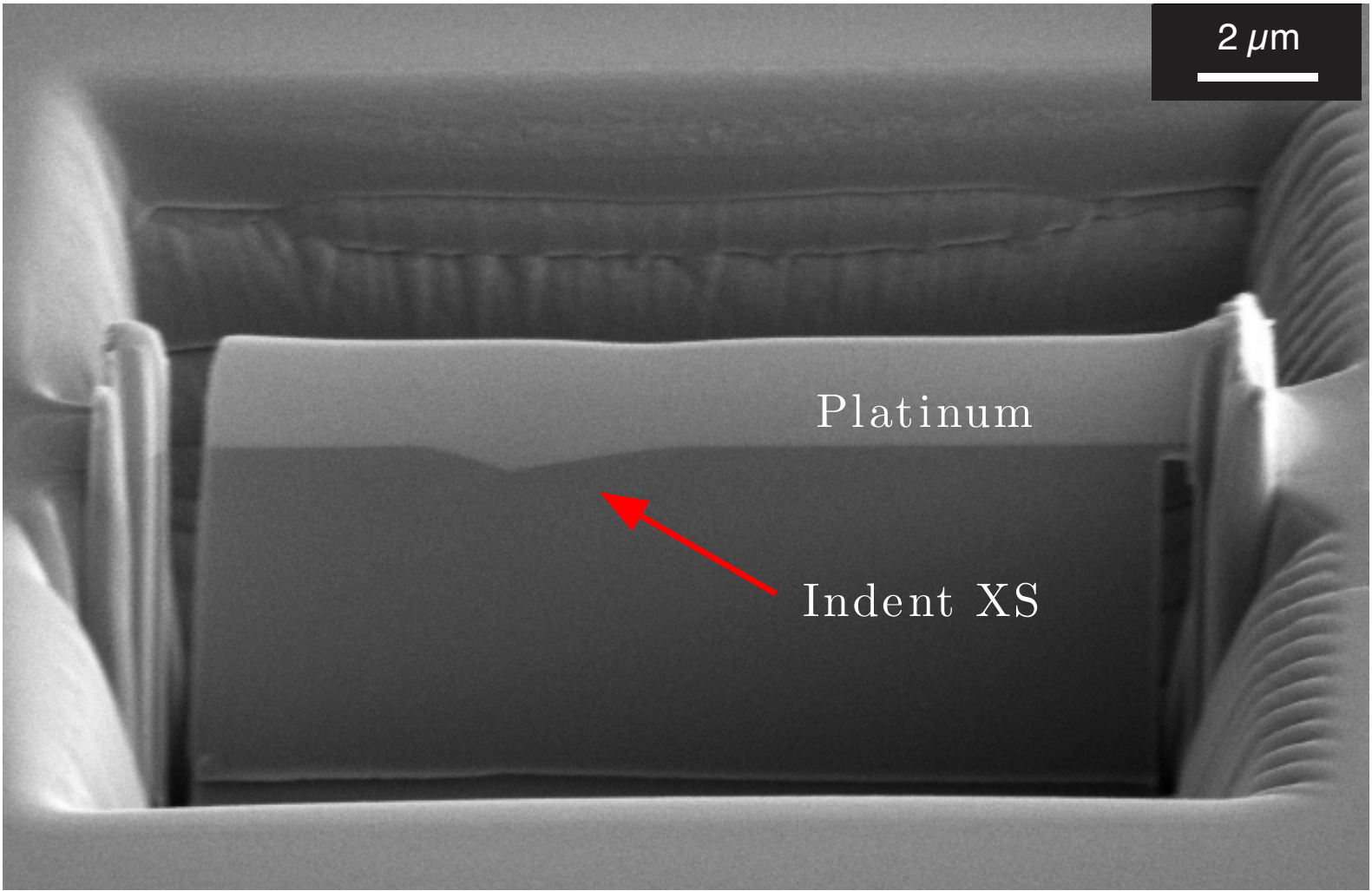

***Figure(s) 2**

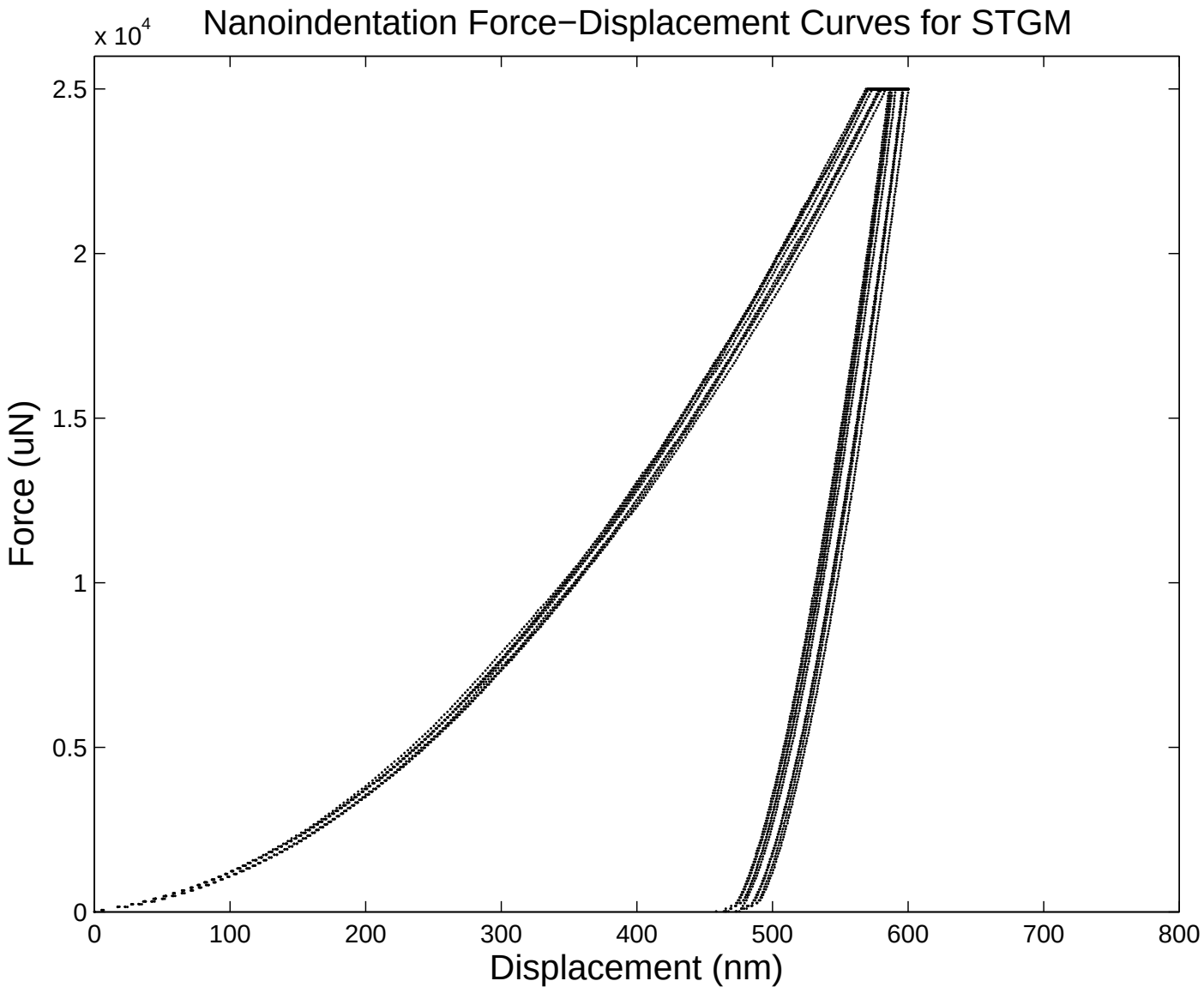
Nanoindentation Force−Displacement Curves for STGM
x 10^4
2.5
2
1.5
1
0.5
0
Force (uN)
0
100
200
300
400
500
600
700
800
Displacement (nm)

*Figure(s) 3

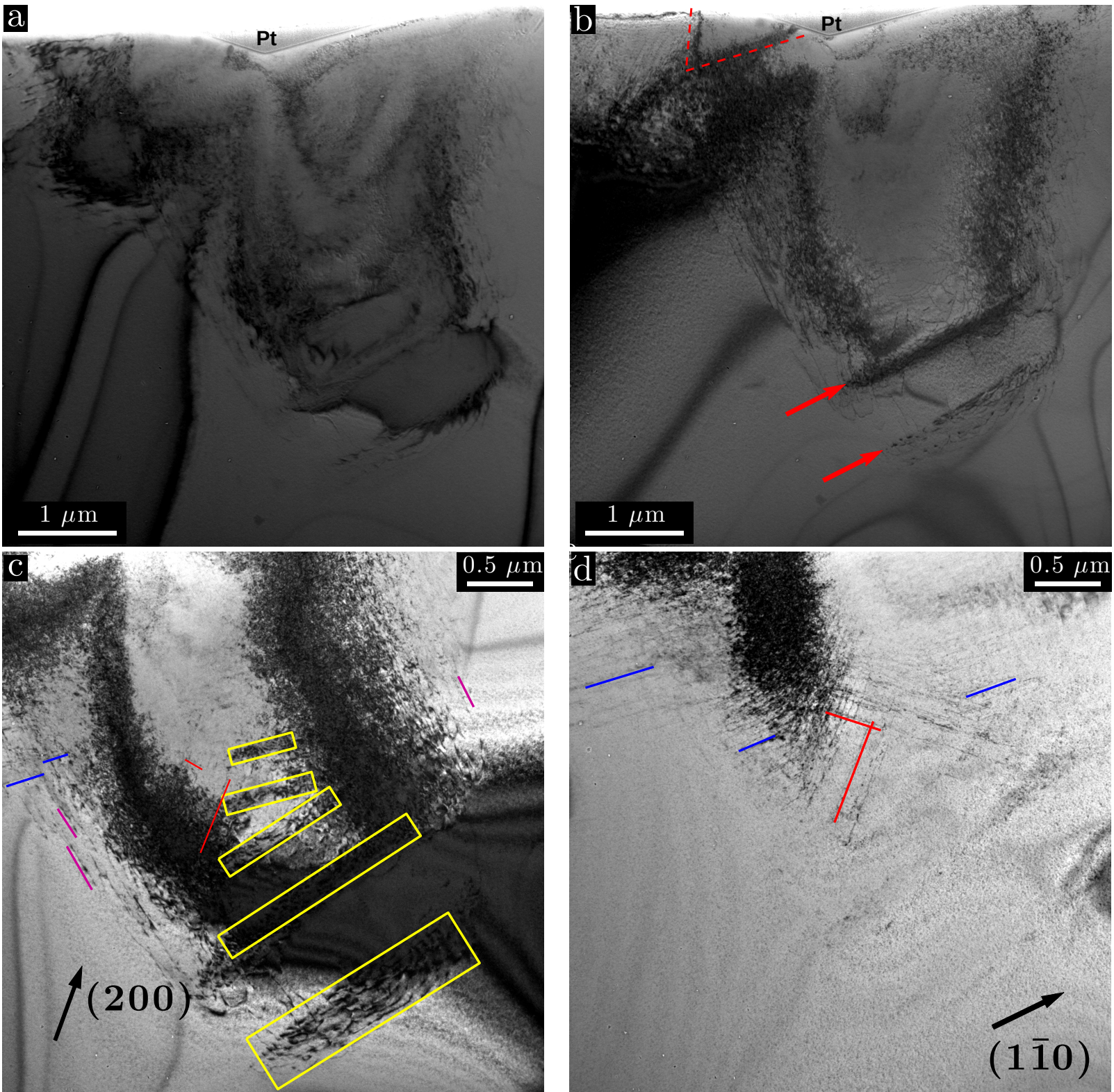

*Figure(s) 4

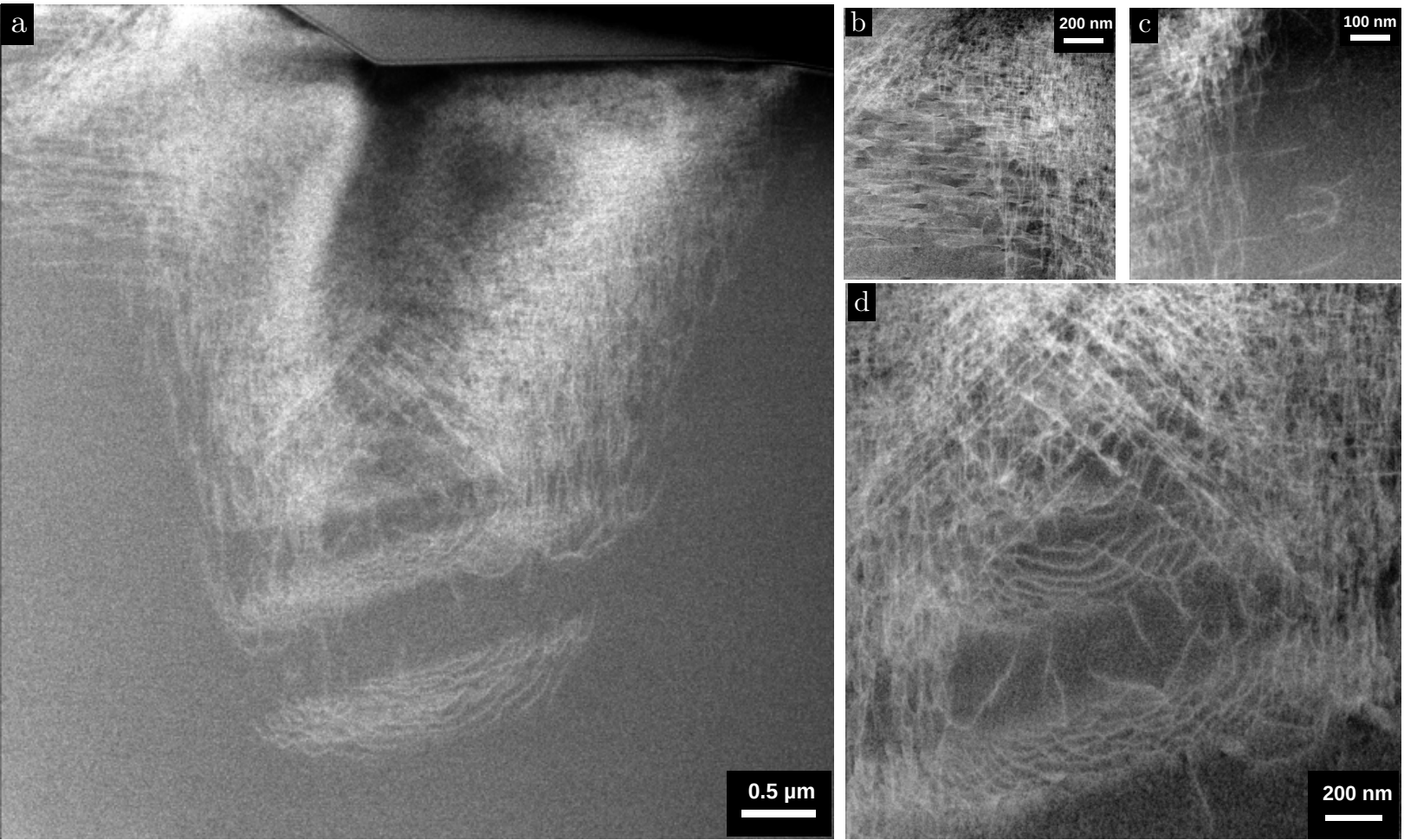

*Figure(s) 5

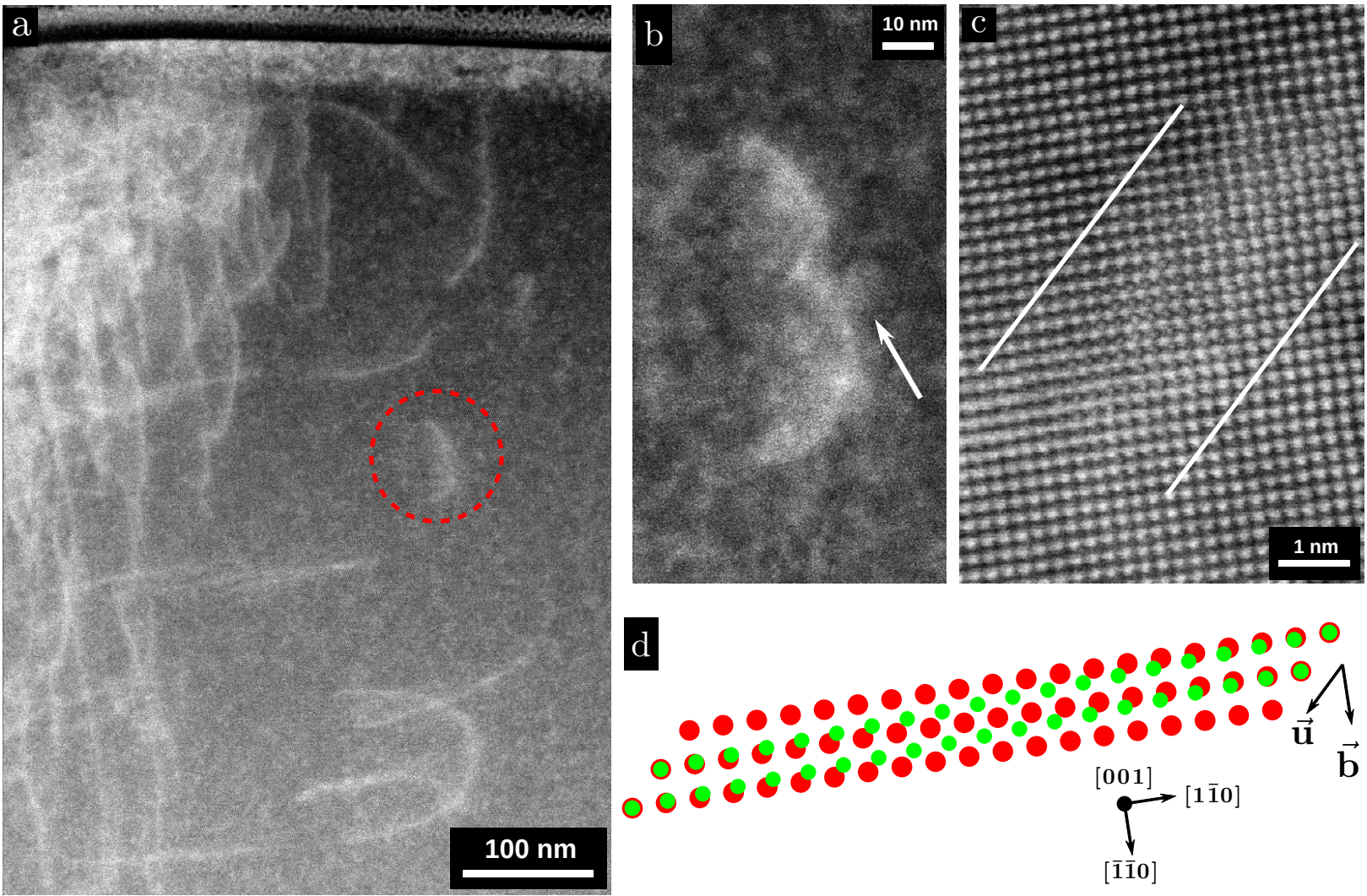

Figure(s) 6

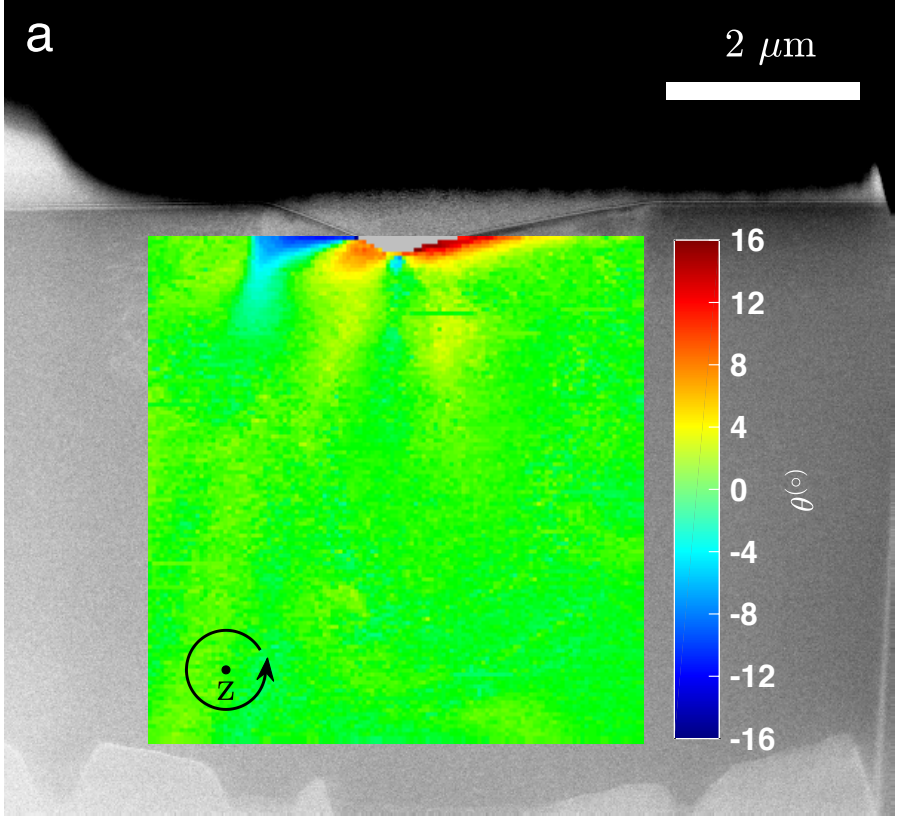
a
2 μm
16
12
8
4
0
-4
-8
-12
-16
θ (°)
z

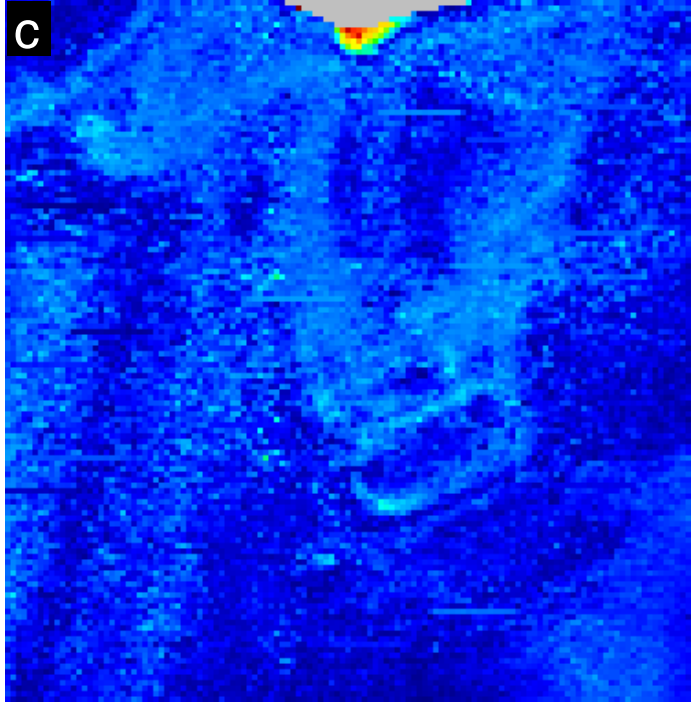
c
0
0.05
0.1
0.15
0.2
0.25
ε_{dev}

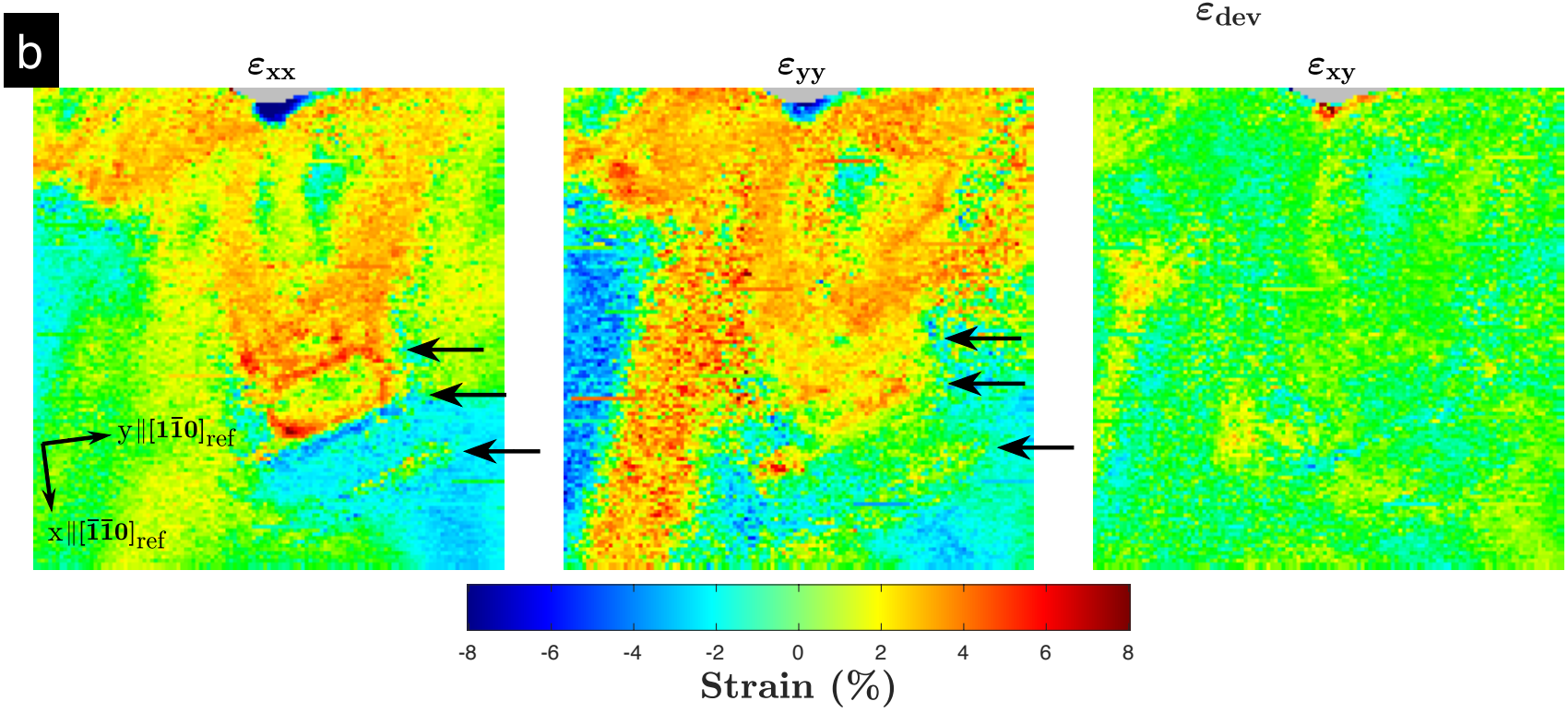
b
ε_{xx}
ε_{yy}
ε_{xy}
y$\|[1\bar{1}0]_{ref}$
x$\|[\bar{1}\bar{1}0]_{ref}$
-8
-6
-4
-2
0
2
4
6
8
Strain (%)

*Figure(s) 7

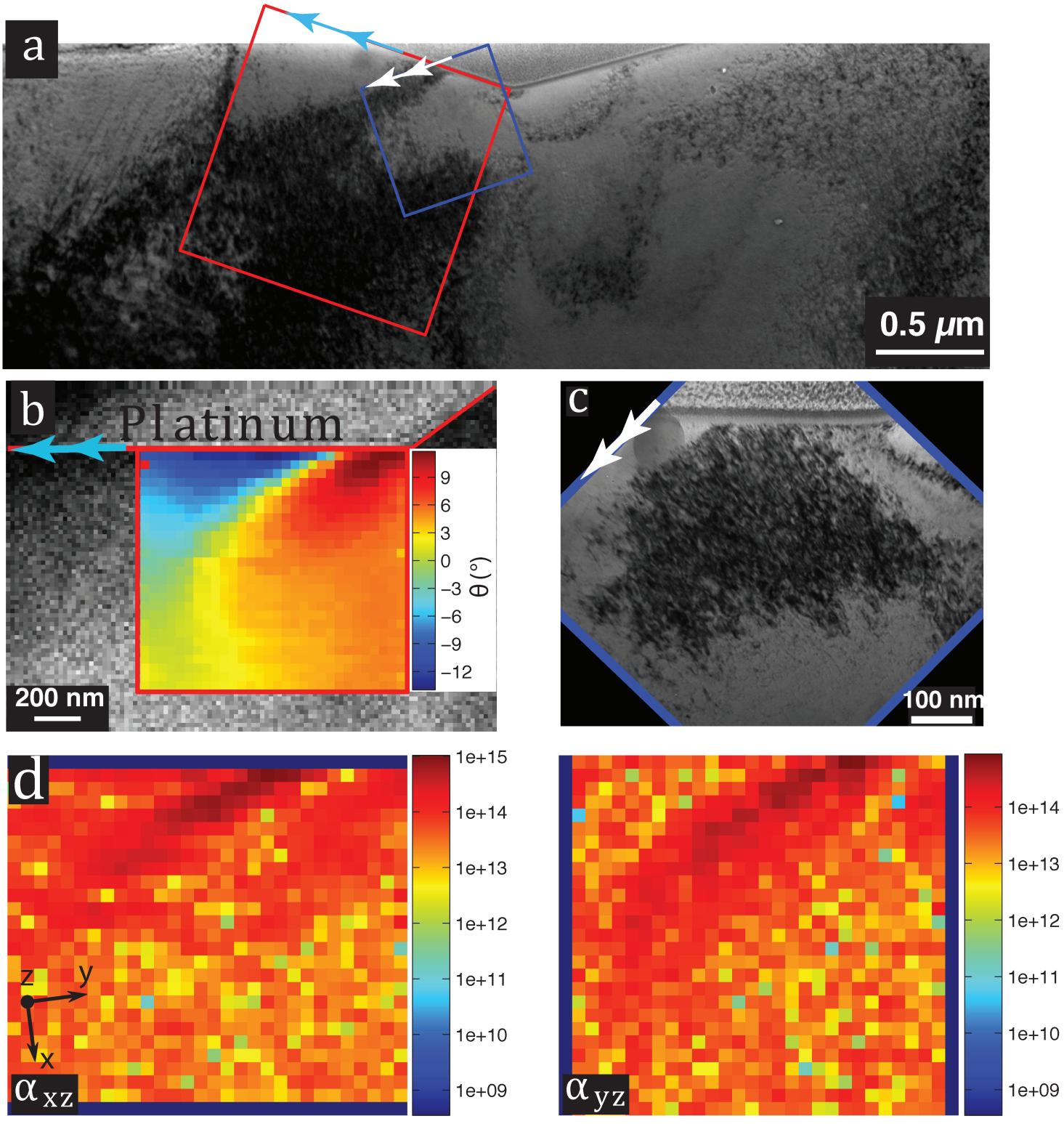
a
0.5 μm
b
Platinum
9
6
3
0
−3
−6
−9
−12
θ (°)
200 nm
c
100 nm
d
z
y
x
α xz
1e+15
1e+14
1e+13
1e+12
1e+11
1e+10
1e+09
α yz
1e+14
1e+13
1e+12
1e+11
1e+10
1e+09

*Figure(s) 8

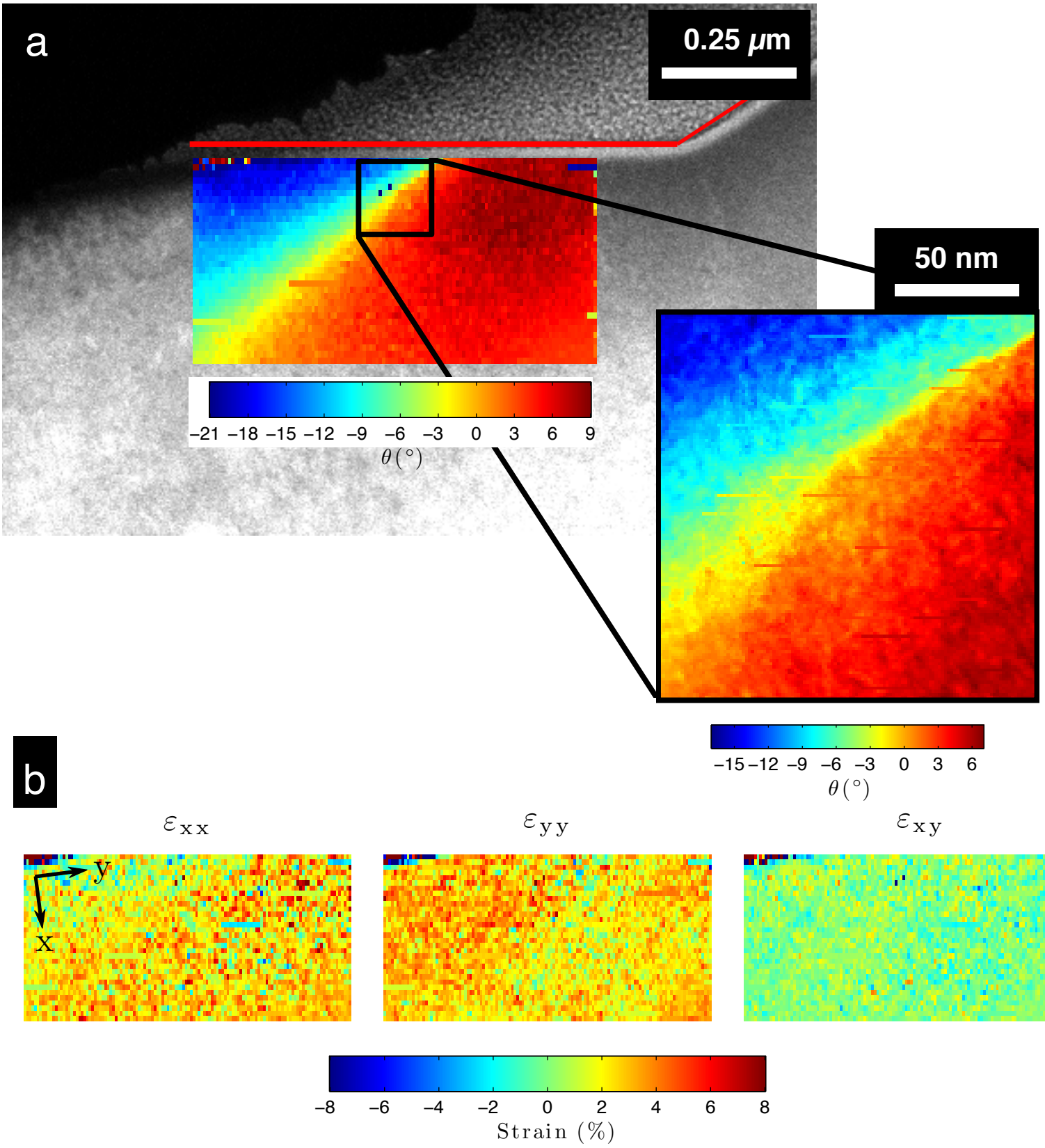
a
0.25 μm
50 nm
−21 −18 −15 −12 −9 −6 −3 0 3 6 9
θ (°)
−15 −12 −9 −6 −3 0 3 6
θ (°)
b
ε xx
ε yy
ε xy
y
x
−8 −6 −4 −2 0 2 4 6 8
Strain (%)

Table(s) 1

Dislocation group	G=200	G= 1-10	G=21-1	G=1-21	G=12-1	Burgers vector, **b**	Sense vector, **u**	Slip System
H	Visible	Visible	--	Visible	Unclear	a/2 [1-11] or a/2[-111]	[1-11]	Screw or [-111](110)
V	Visible	Invisible	Visible	Visible	--	a/2[-1-11]	[-1-11]	Screw
SU	Visible	Visible	--	Visible	--	a/2 [1-11] or a/2[-111]	[200]	[1-11](0-11) or [-111](011)
SD	Visible	Visible	--	Visible	--	a/2 [1-11] or a/2[-111]	[0-20]	[1-11](011) or [-111](101)
	G=200	G=1-10	G=110	G=-21-1	G=1-2-1			
SB	Visible	Invisible	Visible	Visible	Invisible	a/2[111]	Straight segments [1-10]	[111](-1-12)

Table(s) 2

Study	Material	Technique(s)	Indentation Parameters	Observations	Proposed Mechanism
Lloyd et al. (2005)	Cu (FCC)	TEM – SAD (~0.5um step size) TEM imaging	Nanoindentation Load: 5mN Indentation direction: <001>	-Lattice rotations adjacent to indent	Martensitic shuffling: calculated effective GND up to $2.5*10^{15}/m^2$
Kysar et al. (2007)	Cu, Al (FCC, single crystal)	EBSD: 3-5um step size	Indentation – Wedge Depth: 400, 750nm Indentation direction: [00-1] with wedge parallel to [110]	-Lattice rotation discontinuities adjacent to indent (counter rotational lobes present, separated by rotation free areas)	Dislocation slip: Calculated GND up to $\sim 8*10^{14}/m^2$
Zaafarani et al. (2007)	Cu (FCC)	EBSD: 80nm step size	Nanoindentation - Conical Depth: up to 1um Indentation direction: <111>	- Six counter rotational lobes adjacent to indent separated by rotation free areas	Dislocation slip: counter rotational lobes due to changing loading axis activating different slip systems
Rester et al. (2007)	Cu (FCC, single crystal)	EBSD: 20nm step size TEM imaging of dislocation arrangement	Nanoindentation - Berkovich Load: 2.5-10mN Depth: 300nm Indentation direction: <111>	-Counter rotational "zones" adjacent to indent, no obvious rotational free zones -Subgrain formation beneath indenter tip	Dislocation slip: lobes produced by dislocation pile-up forming small angle grain boundary structures
Present study (2017)	Solution Treated Gum Metal (BCC, 50-100um grain size)	TEM - NPD: 40nm, 13.4x7.6nm, 1.2nm step sizes TEM/STEM imaging of dislocation arrangement, g.b analysis	Nanoindentation - Berkovich Load: 25mN Depth: 500nm Indentation direction: <110>	-Four counter rotational lobes adjacent to indent, continuous rotation, no presence of rotation free areas -Dislocation arrangement -Shear bands -Small angle grain boundaries	Dislocation slip: Continuous lattice rotations accommodated by large GND up to $\sim 10^{15}/m^2$

Supplementary Material

Click here to download Supplementary Material: RPSankaran_Supplementary Materials_Acta Mater.docx

Supplementary Material Figure 1

Click here to download Supplementary Material: Supplementary_Figure_01.pdf

Supplementary Material Figure 2

Click here to download Supplementary Material: Supplementary_Figure_02.pdf

Supplementary Material FIgure 3

Click here to download Supplementary Material: Supplementary_Figure_03.pdf

Supplementary Material Figure 4

Click here to download Supplementary Material: Supplementary_Figure_04.pdf

*Graphical Abstract